Prototype design of satellite payload for neutron spectrum acquisition

Xiao-Li Wang,[1,2] Shu-Cheng Shi,[1] Chen-Yao Han,[1,*] Yi-Ming Ma,[1] Quan-Qi Shi,[1,†] Shuai Wang,[1] and Jiao Feng[1]

[1]*Shandong University, Weihai 264209, China*

[2]*Shandong University–Weihai Research Institute of Industrial Technology, Weihai 264209, China*

In recent years, there have been fewer missions to detect neutrons in the low Earth orbit (LEO), and the data obtained have been extremely limited. Studying the distribution of the neutron energy spectrum in LEO through detection can help to solve three major scientific problems: the source of particles in the inner radiation belt, information on solar accelerated particles and the proportion of neutrons from different sources in near-Earth space. The detection efficiency and accuracy of neutrons are affected by the charged particles and primary particles in the environment and the secondary neutrons produced by the spacecraft itself, which has been a hot research topic. The neutron spectrometer developed in this paper adopts two combinations of 15 silicon detectors in terms of detector type and arrangement, which are used for neutron detection by nuclear reaction method and recoil proton method, respectively, in which 27 μm-thick ^{6}LiF conversion layer is used for thermal neutron detection up to 0.4 eV and 300 μm-thick high density polyethylene (HDPE) conversion layer is used for fast neutron detection up to 14 MeV and below. The design of the detector set can also remove the influence of primary charged particles and secondary neutrons in the environment to be detected to a certain extent, improving the accuracy of neutron detection. This paper has completed the neutron spectrometer hardware, firmware, software design, and the basic performance of the front-end readout chip SKIROC2A was tested, the readout circuit of each channel baseline ADC code is less than 17, so the channel consistency is good. The RMS noise of the channel baseline is only 7.1 mV and has good stability. The maximum number of events that can be processed per second is 75. The overall power consumption is 3 W, weight is 792 g, and volume is less than 1 dm^3. In addition, the neutron spectrometer was tested for principle and detection efficiency using various neutron sources such as ^{241}Am-Be neutron source, 2.5 MeV neutron beam current, 14 MeV neutron beam current, etc., and the experiments were analyzed with corresponding simulations. The experimental data and the simulation results are in good agreement and meet the design expectations. The intrinsic detection efficiency of the probes used in neutron spectrometer is 1.05% for 14 MeV fast neutrons.

Keywords: neutron spectrometer, satellite payload, prototype design, Geant4, SKIROC2A

I. INTRODUCTION

There are many sources of neutrons in near-Earth space. For example, galactic cosmic rays [1] can reach the vicinity of Earth and produce neutrons; The solar high-energy particle event [2] reaching the Earth's atmosphere [3] triggers secondary neutrons, which are detected by ground-based neutron monitors. secondary neutrons produced by the interaction of spacecraft materials with solar energetic protons, galactic cosmic rays, and locally trapped protons in the radiation belts [4]; solar neutrons produced by the interaction of solar protons and heavy ions with the Sun's atmosphere [5, 6]; Flash neutrons produced by the interaction of lightning energetic gamma rays interacting with the Earth's atmosphere [7, 8]. Detection of neutrons in near-Earth space by neutron spectrometer can help solve three major scientific problems. These include the study of the radiation sources of particles in the inner radiation belts [9]; the study of the mechanism of solar neutrons on the study of particles accelerated by solar flares [10]; The study of the percentage of neutrons from different sources in near-Earth space, which can be analyzed in comparison with the lightning observation data on the ground.

The current mainstream view is that cosmic ray albedo neutron decays are one of the sources of protons in the inner radiation belts, although it was previously thought that the electron fluxes at different locations in the radiation belts differed greatly and that there would be other sources [11]. But the measured data from the low Earth orbit (LEO) by Li et al. [12] in 2017 show that the albedo neutron decay is a stable source of electrons in the radiation belts. So the neutron spectrometer data is promising to provide reliable observational evidence as a supplement or explanation to the theory. The current observation of solar neutron events is mainly based on the construction of large neutron detectors at high altitude and low latitude areas on the ground [13]. The neutron spectrometer can directly detect solar neutron events outside the Earth's atmosphere, thus eliminating the influence of the Earth's atmosphere and helping to detect weaker solar neutron events [14], with clearer detection signals, and can even observe solar neutron events during periods of relatively infrequent solar activity. In addition, the neutron spectrometer can also detect neutrons produced by Earth's lightning, and in combination with lightning observation base station data on the ground [15], study the contribution of lightning to neutrons in near-Earth space [16, 17].

Because the radiation environment of LEO is more complex, there are many kinds of high-energy charged primary particles will have many kinds of nuclear reactions with the neutron detector itself to produce secondary neutrons. The neutron detection itself needs to exclude the influence of many kinds of errors, so in recent years there are fewer neutron detection missions for LEO. In 1989, Keith et al. [18] used various neutron detectors to detect neutrons in LEO. For

* Chen-Yao Han, chenyao.han@mail.sdu.edu.cn

† Quan-Qi Shi, sqq@sdu.edu.cn

thermal neutrons, a 50 μm Gd shield and other elements with a large neutron capture cross section were used. Fast neutrons were measured using a Bonner ball detector. The complex structure of the detector resulted in a bulky system. In 1991, Dudkin et al. placed several neutron detectors on the Mir space station to measure the neutron energy spectrum in LEO [19], relying on nuclear latex and organic scintillator detectors containing ^{6}Li, with a more conventional data-processing system, which is not able to satisfy the scenario of real-time data and a large neutron differential flux. In the same year Korf et al. [20] used organic scintillators to detect neutron differential flux spectra in the Earth's atmosphere, using plastic scintillator wraps for anti-consistency. However, the plastic scintillator needs to be shielded from gamma, resulting in a larger volume and poorer energy resolution. In 2001, Lyagushin et al. [21] used a nuclear latex detector and a nuclear fission foil to detect LEO neutrons inside the Mir space station module, which is more efficient for fast neutrons but sensitive to gamma ray interference, which can easily lead to false triggering. Fissile material usually requires a certain amount, resulting in a large detector size. In the same year, Matsumoto et al. [22] used the Bonner ball detector to detect neutrons on the ISS, in which the ^{3}He tube detector used is large and fragmented, which is not very suitable for space payload miniaturization equipment. Moreover, the detection efficiency of the ^{3}He tube detector for neutrons varies with the neutron energy, so the pre-calibration work is very tedious.Recently, the China Space Station has seen the installation of an Energy Particle Detector(EPD), which features the innovative use of CLYC (Cs_2LiYCl_6:Ce) as a neutron measurement sensor [23, 24]. This marks the first application of this material in space detection.

It can be seen that the current space neutron detection equipment is generally too complex and bulky, resulting in high power consumption, which is not suitable for long-term data acquisition on compact satellites. With the development of semiconductor detectors [25, 26], integrated forward chips [27, 28] and high-speed data acquisition and processing systems [29, 30], it is possible for space neutron detection payloads to achieve long-time operation, high detection efficiency and high anti-jamming capability on the basis of ensuring low-power miniaturization [31, 32].

For applications of neutron detection in LEO, a neutron spectrometer [33, 34] has been constructed by our group. The neutron spectrometer is based on Si detectors [35, 36], using ^{6}LiF [37, 38]and high density polyethylene (HDPE) [39, 40] as neutron conversion layer for the detection of thermal neutrons (¡0.4 eV) and fast neutrons (¡14 MeV). The power consumption of the neutron spectrometer as a whole is 3 W, which combined with the power consumption assigned by the satellite, is expected to run continuously for one year in orbit. The overall weight is 792 g and the volume is less than 1 dm^3. The neutron spectrometer onboard the "Weiming-1" CubeSat was launched in January 2024, in Sun-synchronous orbit at an altitude of about 530 km. So far, on-orbit data of the neutron spectrometer continues to be accumulated and processed.

II. SYSTEM COMPOSITION

A. Detector selection

Si detectors have low density, low leakage current, small size and high energy resolution. It is widely used in the field of particle detection. Therefore, in this paper, 15 Si detectors with effective area circle diameters of 35 mm and 28 mm and a thickness of 300 μm are designed as the detectors of the particle detection system. It can be ensured that the particles in the pre-detection energy range produce sufficient deposition energy in the detectors [41, 42]. The specific package dimensions of the two Si detectors are shown in Fig. 1.

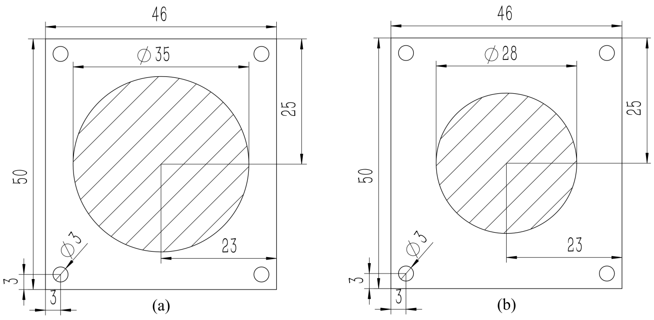

Fig. 1. Detector dimensions: (a) 35 mm, and (b) 28 mm

B. Arrangement of detectors

For neutron detection in space, the radiation environment where the detector is located is complicated. Both charged particles and neutrons exist in space, so the interference of charged particles needs to be eliminated by the method of anti-coincidence. Fig. 2 shows a schematic diagram of the anti-coincidence structure, where the upper and lower detectors have larger areas, while the middle detector has a smaller area. The blue color is the conversion layer [42]. Anti-coincidence means that if there is a signal in detector A or C at the same moment, the signal in detector B at this moment is removed.

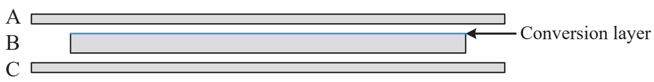

Fig. 2. Schematic diagram of anti-coincidence structure

The neutron spectrometer will detect thermal neutrons and fast neutrons up to 14 MeV. To improve the detection efficiency and to remove the influence of charged particles, the thermal neutron section uses a total of six detectors and a Gd shielding consisting of an anti-coincidence detector set. The fast neutron section uses nine detectors, one of which is shared by fast and thermal neutrons. The neutron spectrometer detector arrangement is shown in Fig. 3, with a total of 15 silicon semiconductor detectors [42].

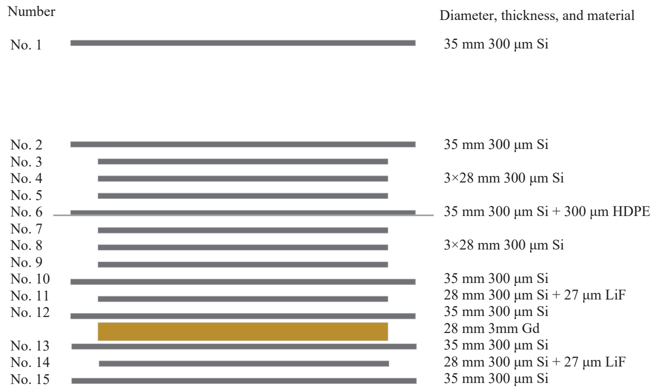

Fig. 3. Neutron spectrometer 15-chip detector set

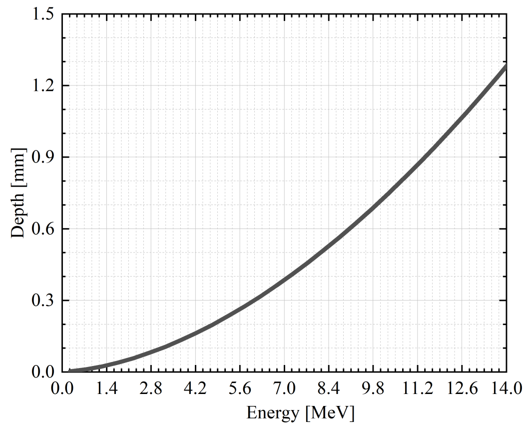

Fig. 4. Detector thickness required for full deposition of fast neutrons below 14 MeV at vertical incidence

There are 15 silicon semiconductor detectors with a thickness of 300 μm. Detector No. 6 is covered with a 300 μm-thick HDPE conversion layer. Detectors No. 11 and No. 14 are covered with a 27 μm thick LiF conversion layer. Detectors No. 3, No. 4, No. 5, No. 7, No. 8, No. 9, No. 11, and No. 14 have an effective area circle with a diameter of 28 mm. Detectors No. 1, No. 2, No. 6, No. 10, No. 12, No. 13, and No. 15 have an effective area circle with a diameter of 35 mm.

Detector No. 1 is used to identify the direction of incoming probe particles. Detectors No. 2–No. 10 are fast neutron detectors, of which No. 3, No. 4, No. 5, and No. 7, No. 8, No. 9 have the same thickness and effective area, the only difference is that there is a 300 μm-thick high-density polyethylene fast-neutron converter layer in front of No. 7, No. 8, and No. 9, and the detectors No. 3, No. 4, and No. 5 can detect signals generated by galactic cosmic rays or other secondary neutrons, while the recoil proton detectors No. 7, No. 8, and No. 9 can also detect the recoil proton signals generated by orbital neutrons passing through the high-density polyethylene conversion layer. Therefore, under the anti-coincidence condition, the recoil proton spectrum can be obtained by subtracting the total energy spectra of detectors No. 7, No. 8, No. 9, and silicon detectors No. 3, No. 4, No. 5, and this symmetric structure can effectively reduce the influence of background signals on the measurements, and improve the accuracy of the neutron energy spectrum inversion. The thickness of the 3-layer recoil proton detector is about 900 μm, which allows complete deposition of protons up to 14 MeV considering oblique incidence. Fast neutrons are detected by the recoil proton method and the fast neutron energy spectrum is obtained by the least squares method, a neutron inversion algorithm [44]. The results of the simulation using Geant4 are shown in Fig. 4.

Detectors No. 10–No. 15 are thermal neutron detectors. Detectors No. 10, No. 12, No. 13, and No. 15, which have larger areas, are used as anti-coincidence detectors, so that charged particle signals in a wide range of stereo angles can be removed by anti-coincidence. A 3 mm-thick sheet of Gd is placed between detectors No. 12 and No. 13 to absorb thermal neutrons, so that detector No. 11 with the ^{6}LiF coating can record the counts of the signals generated by the reaction of neutrons in the omnipotent band with ^{6}LiF. The following detector No. 14 with ^{6}LiF coating mainly records the counts of signals generated by the reaction of neutrons other than thermal neutrons with ^{6}LiF, and the thermal neutron flux in the orbit can be obtained by dividing the difference in counts between the two detectors by the detection efficiency. In addition, to distinguish the source direction of thermal neutrons in LEO to a certain extent, a piece of 3 mm-thick Gd is also placed around the detector array, except for the remaining five faces of the open side, to block the thermal neutrons from other directions [44], and the specific position of Gd is shown in Fig. 5.

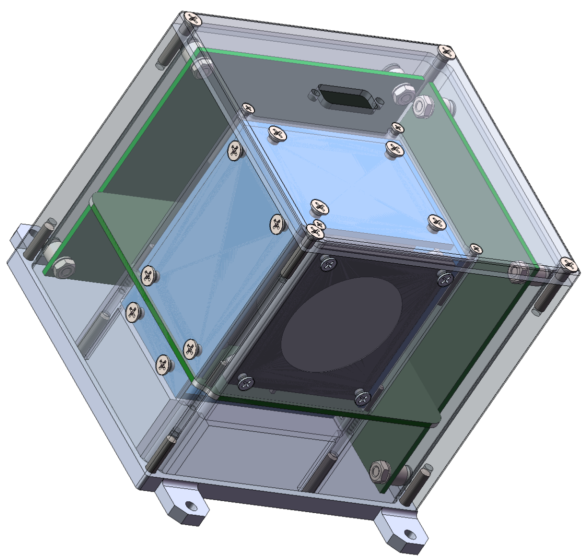

Fig. 5. Gd placed on 5 faces around the detector

The blue part is the 3 mm-thick Gd placed on the five faces around the detector combination. Since the capture cross sections of thermal neutrons are different for different Gd isotopes, and the reaction cross sections of neutrons and ^{6}Li are different for different energies, to analyze the effect of Gd

on thermal neutron detection at different energies, the Si detectors with LiF coatings that are blocked by Gd and those that are not were simulated by using Geant4 simulations to study the variation of the detection efficiency of the detector for thermal neutrons with thermal neutron energy in both cases [44], as shown in Fig. 6.

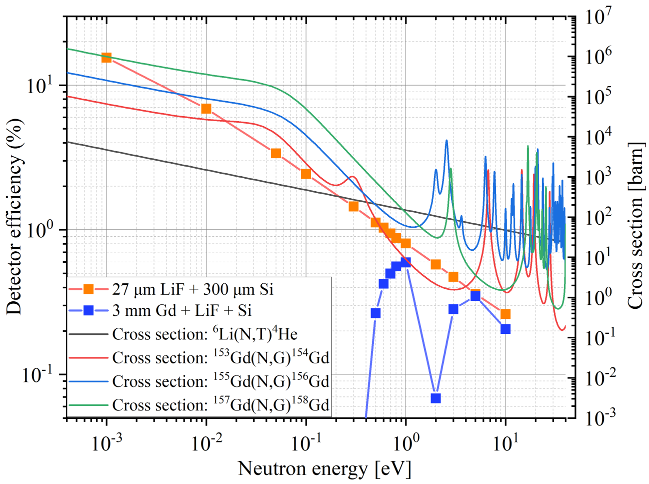

Fig. 6. Effect of Gd on thermal neutron detection at different energies

Orange data points are the detection efficiency of detector No. 11 for different energies of neutrons as a function of neutron energy, blue data points are the detection efficiency of detector No. 14 for different energies of neutrons as a function of neutron energy, grey lines are the reaction cross sections of ^{6}Li (N,T) ^{4}He as a function of neutron energy. The other lines are the reaction cross sections of neutrons captured by various Gd isotopes as a function of neutron energy. For thermal neutrons with energies lower than 0.4 eV, the 3 mm-thick Gd can completely block them. The blocking effect of Gd on neutrons of different energies will be taken into account as a function of the detection efficiency in subsequent calculations of the orbital thermal neutron flux using neutron spectrometer data.

III. SYSTEM DESIGN

A. Hardware design

The hardware design of the neutron spectrometer consists of three circuit boards, namely the power supply board, the front-end board and the data board. The power supply board is designed as a low-noise power supply module, which is responsible for supplying power to all parts of the neutron spectrometer and generating the bias high voltage required for detector operation. The front-end board connects to the detector and uses the SKIROC2A chip as the core of the front-end readout system. The SKIROC2A is a 64-channel front-end ASIC designed to read out the signals from the silicon detector. The data board contains FPGA, MCU and memory chips.

The physical diagram of the neutron spectrometer is shown in Fig. 7. The overall hardware block diagram is shown in Fig. 8.

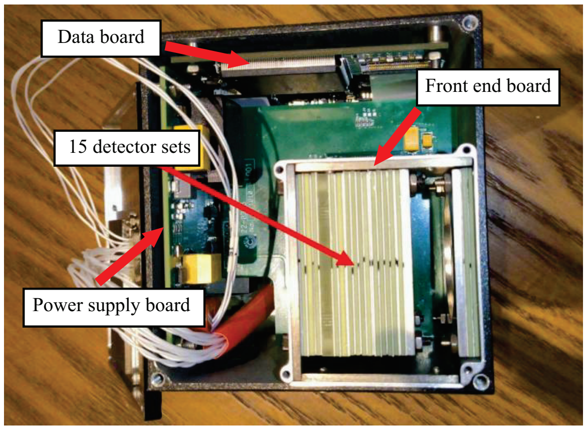

Fig. 7. Physical view of neutron spectrometer

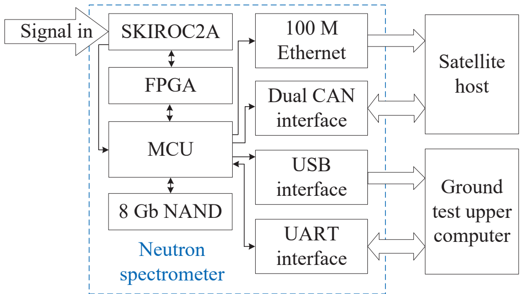

Fig. 8. Block diagram of neutron spectrometer hardware

The signals from the detector are directly transmitted to SKIROC2A, then SKIROC2A converts the analogue signals to digital signals and passes them to the FPGA for data processing, and finally the FPGA passes the processed data to the MCU. At the same time, some of the signals in SKIROC2A are directly connected to the MCU. The MCU is mounted with a CAN interface chip, Ethernet interface, USB interface, UART interface and SD NAND. The MCU is equipped with CAN interface chip, Ethernet interface, USB interface, UART interface and SD NAND. CAN interface and Ethernet interface are used to communicate with the satellite host, CAN transmits commands and telemetry signals, and Ethernet interface is used to transmit scientific data.

B. Firmware design

The firmware design part of the neutron spectrometer was implemented using the Cyclone series FPGA from Altera. The main purpose of this part is to control SKIROC2A and packetize data. Since the data format of SKIROC2A cannot be changed, the neutron spectrometer only uses 15 of the 64 channels of SKIROC2A, so there is a lot of invalid

information in the data packet. To reduce the bandwidth pressure and storage pressure, it is necessary for the FPGA to sort out the valid information from the memory map of SKIROC2A and organize it into data packets, which are ultimately passed to the file management system of the MCU for storage. The firmware design part of the FPGA consists of a number of modules, including a clock module, a trigger module, a timing control module, a data acquisition module, and an SPI module. The block diagram of the main modules in the firmware design section is shown in Fig. 9.

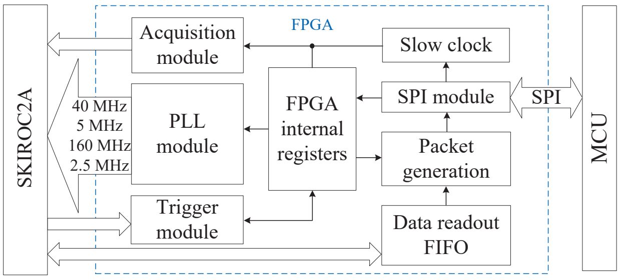

Fig. 9. Firmware design module block diagram

The clock module generates clock frequencies of 40 MHz, 5 MHz, 160 MHz, and 2.5 MHz, of which 40 MHz and 5 MHz are the clock frequencies used in normal operation, and 160 MHz and 2.5 MHz are the frequencies used in testing. The trigger module is the module used for test calibration. When SKIROC2A generates a trigger signal, the trigger module can control the external ADC to perform A/D conversion of the charge stored in SKIROC2A. Since the external ADC is not used during normal operation, the module is idle. The timing control module needs to receive and save the slow control signal for MCU conversion. Before starting the acquisition, the module sends the stored slow control commands to SKIROC2A and controls the timing of the single-ended signals. The data acquisition module is used to temporarily store the memory map of SKIROC2A, extract valid data and organize them into packets. The SPI module is used for communication between the FPGA and the MCU.

C. Software design

The software design of the neutron spectrometer is realized by using the MCU of STM32 series and FreeRTOS. The block diagram of the software design is shown in Fig. 10.

The software design contains four main task threads. They are the FPGA communication processing thread, the interface communication thread, the memory system thread and the instruction analysis and telemetry generation thread. In addition to what is shown in the figure, the MCU program also includes basic programs such as watchdog subroutine and clock subroutine.

The FPGA communication processing thread is used to communicate with the FPGA, which includes SPI initialization, slow control command generation, data processing and data saving. The interface communication thread is used

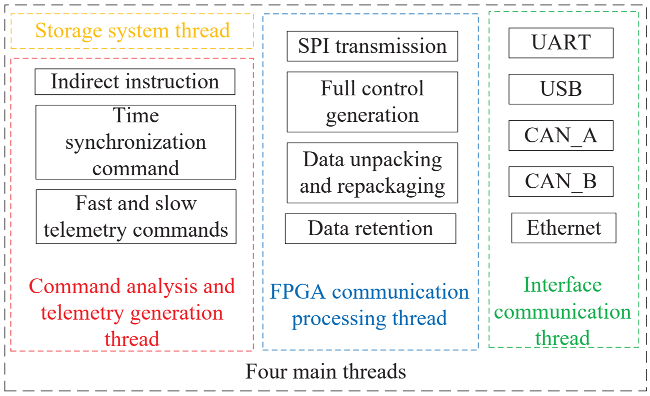

Fig. 10. MCU combined with FreeRTOS software design of the four main threads

to control the interfaces with external devices, including the USB and UART interfaces for ground test, the two CAN interfaces for connecting to the satellite, and the Ethernet interface for direct digital transmission with the satellite. The storage system interface is used to drive the SD NAND flash memory inside the neutron spectrometer and provide file system services, and the file system adopts FAT32. The command analysis and telemetry generation thread is used to analyze the commands in the CAN and control other threads. The Star Control Center computer sends fast- and slow-change telemetry polling control sequences over the CAN bus to obtain the operating status of the neutron spectrometer.

IV. SYSTEM TESTING AND ANALYSIS

A. Basic performance test

After completing the hardware, firmware and software design of the system, it is first necessary to test and verify whether the basic performance of the neutron spectrometer meets the design requirements. This includes the baseline noise RMS and stability of the neutron spectrometer, the consistency between channels and other basic parameters. In this paper, the front-end board is connected to the detector, and the SKIROC2A chip is used as the core of the front-end readout system, so it is necessary to ensure the baseline RMS noise and stability of the 64 channels of the SKIROC2A and the consistency between the channels, which will greatly affect the measurement of deposition energy spectrum. In the baseline test, this paper sets the threshold value to 255, when the threshold value is close to the baseline reading of the ADC, the trigger circuit continuously generates a trigger signal, acquires and records the baseline signal of the 64 channels, and converts it to a numerical value through the internal ADC. Then the baseline signals of the 64 channels are Gaussian fitted, and the ADC value where the peak is located is taken as the effective value of the channel baseline [45], and the ADC values of the 64 channel baselines are obtained as shown in Fig. 11, with the horizontal axis being the number of chan-

nels Nc, and the vertical axis being the ADC readings of the effective value of the baseline for a period of time.

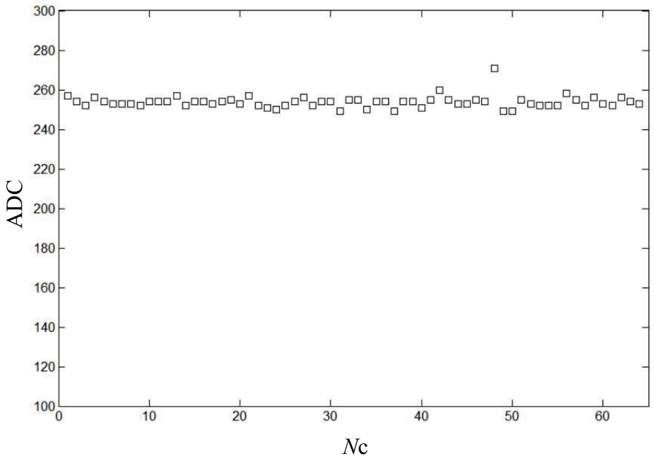

Fig. 11. ADC value of 64 channel baselines

It can be seen that the baselines of most channels are concentrated between 250 and 265, and the baseline difference between different channels is less than 17 ADC values, which shows that the consistency between channels is good. Since the SKIROC2A chip is a 12-bit ADC, and the voltage range is 0.9–2.6 V, the RMS noise of the baseline of all channels is about 7.1 mV and the stability is good. In summary, the baseline RMS noise and stability of the neutron spectrometer, and the consistency between the channels meet the requirements of subsequent experiments.

The average ionisation energy of the silicon semiconductor detector used in the neutron spectrometer is 3.6 eV, i.e., one electron is ionised per deposition of 3.6 eV energy. According to the relationship between the baseline RMS noise and the deposition energy of the silicon semiconductor detector, the minimum deposition energy measurable by the neutron spectrometer can be obtained. The maximum deposition energy measurable by the neutron spectrometer can be obtained by continuously increasing the input signal through the signal generator until the ADC value is saturated. Finally, the electronic part of the neutron spectrometer can handle an energy range of 500 keV-20 MeV [45], and the maximum number of events per second is 75, which meets the requirements of subsequent experiments.

In addition, in the basic performance test, the anti-irradiation performance of the neutron spectrometer is also tested, as the hardware are selected military-grade components, and the software through the operating system for each set of data to ensure the validity of the data. As well as the processing of the bad block of memory, the neutron spectrometer electronics system is guaranteed to work continuously for a long time under the environment of higher irradiation level.

After the completion of the basic performance test of the neutron spectrometer, four major tests will be carried out, namely, thermal neutron principle test, fast neutron detection principle test, fast neutron detection efficiency test and compliance effect test.

B. Thermal neutron detection test

To test the thermal neutron part of the neutron spectrometer in principle, this paper uses the ^{241}Am-Be neutron source from Institutional Center for Shared Technologies and Facilities (INEST) of the Hefei Institutes of Physical Science, Chinese Academy of Sciences to test the Si detector containing LiF coating. The energy spectrum of the ^{241}Am-Be neutron source [46] is shown in Fig. 12, with energies in the range of 0–11 MeV. The primary fast neutrons produced by the neutron source are slowed down by objects such as walls and experimental platforms in the test site, the energy is reduced, and some of the fast neutrons are changed into thermal neutrons with lower energy.

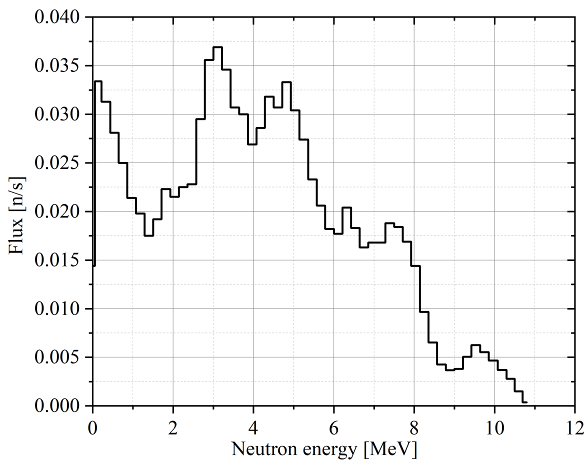

Fig. 12. ^{241}Am-Be neutron source energy spectrum

The detector used in the test is a Si detector with ^{6}LiF coating. The thickness of the sensitive layer of the Si detector is 300 μm. The sensitive area is a circle with a diameter of 28 mm. The thickness of the LiF coating is about 27 μm. The preamplifier used in the experiment is mesytec-MPR-16L and the multichannel analyser is labZY-nanoMCA. The detector is placed in a 2 mm-thick aluminum alloy shielding shell for shading. The copper mesh is used outside the shielding shell to shield the EMI, with the radioactive source and detector positioned at equal heights. The layout of the experimental site is shown in Fig. 13.

The red dots represent the ^{241}Am-Be neutron source. The ^{241}Am-Be neutron source emits neutrons at a steradian angle of π with a flux of about 9×10^{7}/s. The blue part of the back-end experimental platform, which is wrapped in yellow copper mesh, is the neutron spectrometer. To compare the experimental data with the simulation results, the multi-channel spectra obtained from the experiments were energy-scaled. The truncation position at about 2.7 MeV in the deposition spectrum and the starting position of the “platform” at about 1 MeV. The energy spectra from about 1 MeV to about 2.7 MeV were used for the “platform” integration. The “plateau” integrals are used to normalize the experimental data to the simulated energy spectrum, as shown in Fig. 14.

The blue data points are the multi-channel spectral data in

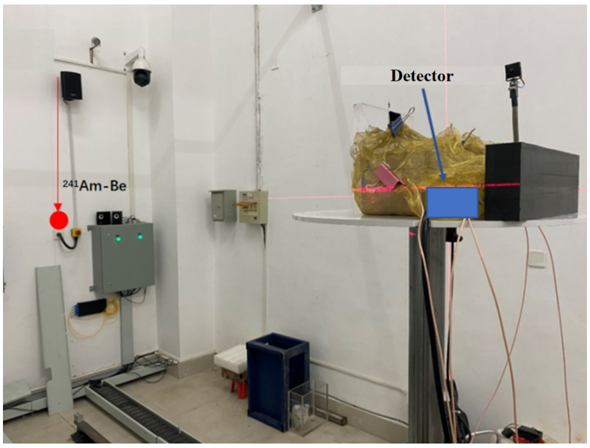

Fig. 13. Experimental environment of the ^{241}Am-Be neutron source

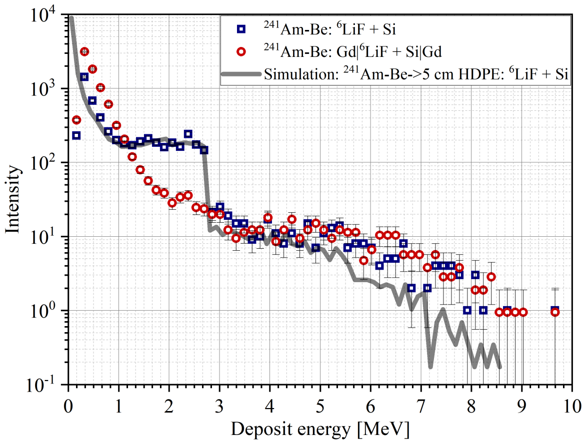

Fig. 14. Testing of LiF-coated Si detectors with thermal neutrons after slowing using the ^{241}Am-Be neutron source

the Si detector obtained by using the LiF-coated Si detector and moving the detector so that the distance between the detector and the radioactive source is about 50 cm; the red data points are the multi-channel spectral data in the Si detector obtained after a period of time based on the experiments in the blue data points, with a piece of Gd with a diameter of 35 mm and a thickness of 3 mm tightly affixed to both sides of the Si detector; the gray line shows the detection effect of the LiF-coated Si detector on the thermal neutrons of the ^{241}Am-Be neutron source slowed down by 5 cm of polyethylene using Geant4. Since it is not easy to simulate and reproduce the slowing down effect of the neutrons by the walls and other objects in the experimental environment, 5 cm thick polyethylene is used as the neutron slowing body placed in front of the detector in the simulation.

For the low-energy part below 1 MeV in Fig. 14, there is some difference between the blue data points and the simulated energy spectrum, and the experimentally measured low-energy deposited particle signal is more than in the simulation and is caused by electrons produced by ^{241}Am-Be neutrons interacting with Gd. The signals considered in the high-energy part of the experiment are not caused by low-energy thermal neutrons, but are produced by ^{241}Am-Be high-energy fast neutrons directly reacting with the Si nuclei in the Si detector. There are three reasons for the inconsistency between the experimental data and the simulated data: firstly, the energy spectrum of the ^{241}Am-Be neutron source input to the simulation is a standard energy spectrum, which is different from the actual energy spectrum [47, 48]. Secondly, since the slowing effect on neutrons by objects such as walls in the experimental environment cannot be easily reproduced by the simulation, a 5 cm thick polyethylene was used in the simulation as a neutron slowing body placed in front of the detector. Finally, there is the effect of the noise signal due to the wobbling of the detector test noise baseline, which is not considered in the simulation [49, 50].

C. Principle tests of fast neutron detection

To perform a principle test of the fast neutron part of the neutron spectrometer, we have tested the Si detector containing a HDPE conversion layer using a 2.5 MeV and 14 MeV neutron beam and the ^{241}Am-Be neutron source from INEST, respectively.

1. Testing with 14 MeV monoenergetic neutron beams

The 14 MeV monoenergetic neutron beam of INEST utilizes the deuterium-tritium reaction T(D,N)^{4}He, and the generated neutrons are emitted outward with a stereo angular distribution of approximately 4π centered on the tritium target target point. A Si detector with a sensitive area of 28 mm diameter and 300 µm thickness was used in the experiment in combination with 300 µm thick HDPE for testing. The preamplifier used in the experiment is mesytec-MPR-16L and the multichannel analyser is labZY-nanoMCA. The experimental site plan and the placement of the Si detector are shown in Fig. 15.

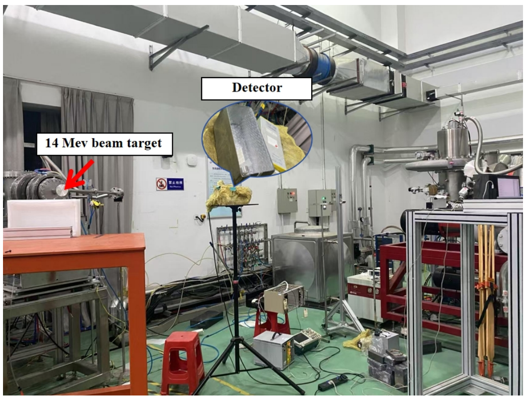

Fig. 15. 14 MeV neutron beam test site

The Si detector position was approximated to be on a horizontal plane with the target about 1.56 m apart, a total of

two control experiments were performed, and the measured multichannel spectral data are shown in Fig. 16.

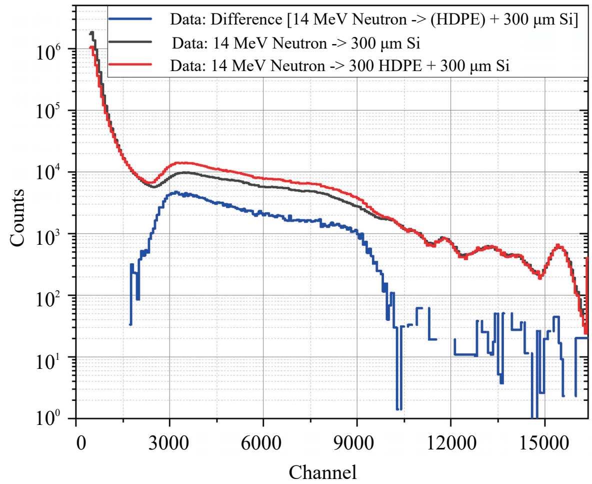

Fig. 16. Data from two control experiments of 14 MeV neutron beam flow

The black line is the multi-channel spectrum generated by 14 MeV neutron direct bombardment of the Si detector, the red line is the multi-channel spectrum generated by 14 MeV neutron bombardment of the Si detector covered with a 300 μm high-density polyethylene conversion layer, and the blue line is the difference between the two, with the black and red lines normalized by the peaks near the last 15,500 channels.

In this paper, to analyze the experimental data, the total deposition energy spectrum produced by a 14 MeV neutron beam current on a Si detector and the effect of a HDPE conversion layer on the total deposition energy spectrum are simulated using Geant4, as shown in Fig. 17.

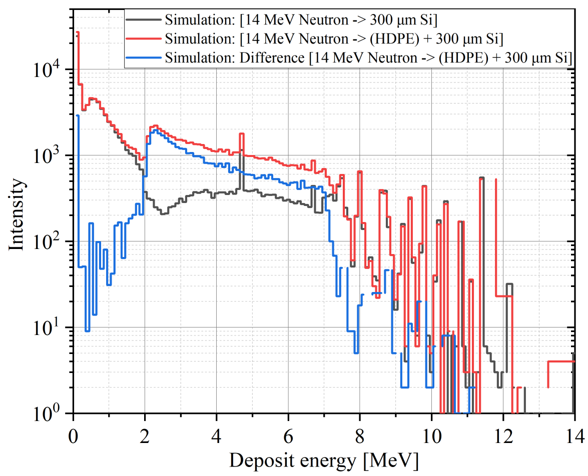

Fig. 17. Experimental data of 14 MeV neutron beam simulation using Geant4

The black line is the multi-channel spectrum produced by 14 MeV neutrons in the Si detector, the red line is the multi-channel spectrum produced by 14 MeV neutrons bombarding the Si detector covered with a 300 μm high-density polyethylene conversion layer, and the blue line is the difference between the two, where the recoil proton signals produced by the reaction between the neutrons and the hydrogen in the high-density polyethylene conversion layer can be clearly seen. The black line in Fig. 16 is the measured multichannel spectrum, and the black line in Fig. 17 is the simulated energy spectrum; they are different because walls and other objects in the environment are not taken into account in the simulation, the problem of energy discrimination in the detector, and the effect of noise signals generated by the wobbling of the detector's test noise baseline during the actual test.

Based on the number of channels at the apex of the left descending edge of the recoil proton multichannel spectrum in the experimental data of Fig. 16 and at the truncation behind it with the energy values of the corresponding positions in the energy spectrum of the recoil proton in Fig. 17 to do the energy scale, the experimentally measured energy spectrum of the recoil proton is obtained, as shown in Fig. 18.

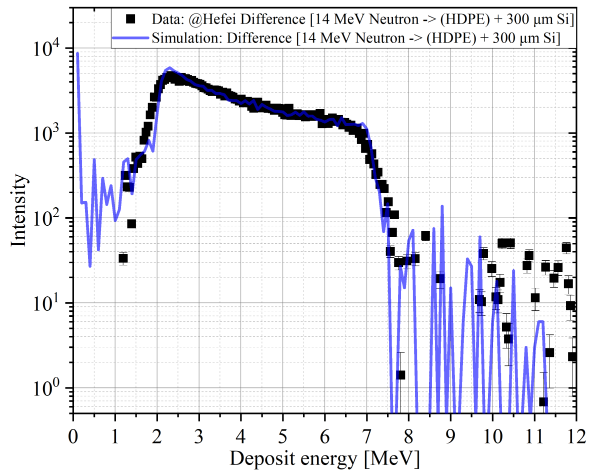

Fig. 18. Deposition energy spectrum of recoil protons in a 300 μm thick Si detector

The black data points are the measured data. The blue lines are the simulation results of Geant4. It can be seen that the experimental data and the simulation results agree well. Since the resolution of the detector is not included in the simulation, the signal peaks of some reactions are narrower than the experimental results.

2. ^{241}*Am-Be neutron source test*

The experimental site is shown in Fig. 13. In this paper, a Si detector with a sensitive region diameter of 35 mm and a sensitive layer thickness of 300 μm was used in combination with a 300 μm-thick high-density polyethylene conversion layer for testing. The preamplifier used in the experiment is mesytec-MPR-16L and the multichannel analyser is labZY-nanoMCA. The multichannel spectrum in the Si detector was recorded after a period of time of measurement, as shown in Fig. 19.

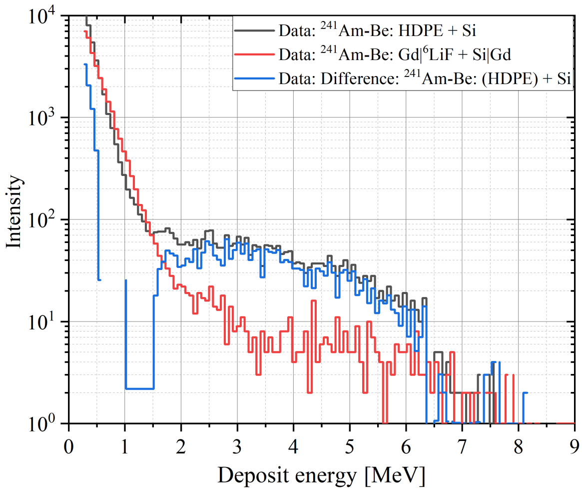

Fig. 19. Testing the fast neutron detection section using the ^{241}Am-Be neutron source

The black line is the deposition spectrum of ^{241}Am-Be neutrons in a Si detector shielded by two 3 mm thick Gd plates, the red line is the deposition spectrum of ^{241}Am-Be neutrons in a Si detector covered by a 300 μm high-density polyethylene conversion layer. The blue line is the difference between the two. The black and red lines are normalised to the energy spectrum integral of 0.5–1 MeV.

The total deposition energy spectrum produced by ^{241}Am-Be neutrons on the Si detector. The effect of the high-density polyethylene conversion layer on the total deposition energy spectrum were simulated using Geant4 and are shown in Fig. 20.

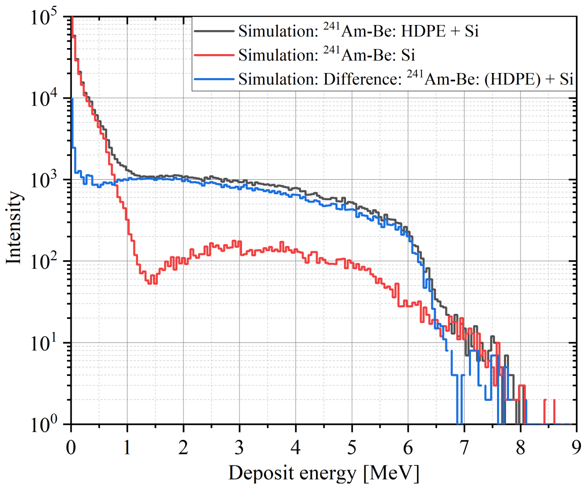

Fig. 20. Total deposited energy spectrum of the ^{241}Am-Be neutron source on a Si detector and the influence of the high-density polyethylene conversion layer on the total deposited energy spectrum

The black line is the deposition spectrum of ^{241}Am-Be neutrons in a Si detector, the red line is the deposition spectrum of ^{241}Am-Be neutrons bombarding a Si detector covered with a 300 μm high-density polyethylene conversion layer. The blue line is the difference between the two. It can be clearly seen that the recoil proton signal is produced by the reaction of neutrons and hydrogen in the high-density polyethylene conversion layer. The measured recoil proton spectrum is compared with the simulation results, as shown in Fig. 21.

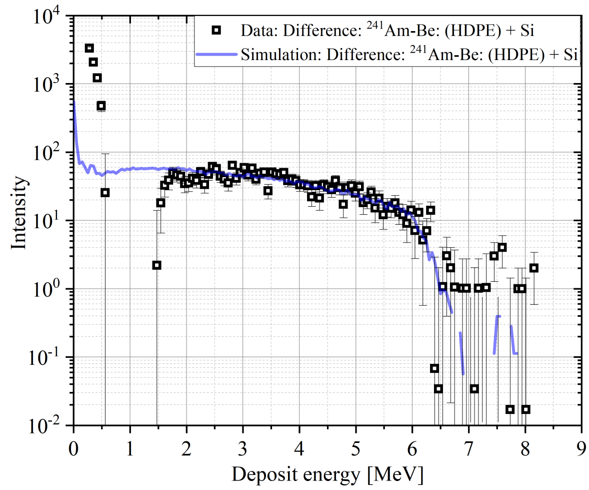

Fig. 21. ^{241}Am-Be neutron source bombarding a 300 μm thick high-density polyethylene conversion layer, resulting in a back-scattered proton deposition spectrum in a 300 μm thick Si detector

The black data points are the measured data. The blue line is the simulation result of Geant4. It can be seen that the experimental and simulated energy spectra between 1.5 MeV and 7 MeV are in good agreement. The reason for the poor agreement in the low-energy part is speculated to be the influence of background noise such as gamma in the experiment, which leads to poor normalization of the data from the two experiments.

D. Fast neutron detection efficiency tests

To test the detection efficiency of the neutron spectrometer for fast neutrons, we used 2.5 MeV and 14 MeV neutron beam currents from INEST to test a 300 μm thick Si detector containing a 300 μm high-density polyethylene conversion layer, respectively. The preamplifier used in the experiment is mesytec-MPR-16L and the multichannel analyser is labZY-nanoMCA.

This paper uses the data in Fig. 16 and Fig. 18 to calculate the detection efficiency of the neutron spectrometer for 14 MeV fast neutrons. The total flux at the target of the neutron source is known. The neutron flux hitting the Si detector is calculated based on the area of the Si detector and the distance from the target. The signal produced by the recoil protons produced by the reaction of fast neutrons with hydrogen nuclei in the conversion layer on the detector is measured, and the number of fast neutrons measured by the fast neutron detector is counted. In the experiment, the Si detector and the target are approximately on the same horizontal

plane, with a linear distance of about 1.56 m. The detector is irradiated with a 14 MeV neutron beam with a flux of 2.3×10^{10}/s. High-density polyethylene is placed in front of the detector and irradiated for 20 minutes to obtain the multi-channel spectrum shown in the black line in Fig. 15. The detection efficiency of the detector for 14 MeV fast neutrons is 1.05%.

Correspondingly, this paper also compares the simulated detection efficiencies at different energy cutoff thresholds, as shown by the brown line in Fig. 22. The black data points are the detection efficiencies measured based on the experimental data, and it can be seen that the experimental data and the simulation results are in better conformity.

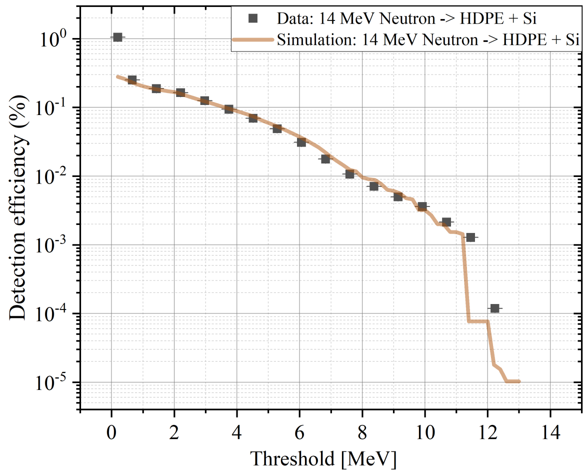

Fig. 22. Detection efficiency of a 300 μm Si detector covered with a 300 μm high-density polyethylene conversion layer for 14 MeV neutrons

E. Coincidence test

To test the compliance effect, the neutron spectrometer was tested at the 14 MeV neutron beam stream at the China Institute of Atomic Energy Sciences (CIAES). The placement of the beam current pipe and the neutron spectrometer at the beam current exit of CIAES is shown in Fig. 23. The neutron beam current reaches the experimental room through the metal pipeline, and there are fewer equipments in the experimental room. The diameter of the beam spot of neutron beam current is also smaller, so the gamma background of the experimental room is less. The opening of the neutron spectrometer is placed directly in front of the exit of the neutron beam pipe, and after a period of irradiation, multi-channel spectra from multiple detectors in the neutron spectrometer are recorded and analysed.

In front of detector No. 7 there is a highly dense polyethylene conversion layer, where neutrons react with hydrogen nuclei in the conversion layer to produce recoil protons of 0–14 MeV [51], which pass through the silicon detector producing deposition energy. In addition, a corresponding simulation was performed in this paper using Geant4 following

Fig. 23. Anti-coincidence test environment

the same experimental configuration. Fig. 24 shows the relationship between the total deposition energy in detectors No. 7 and No. 8 and the deposition energy in detector No. 7 for each event using Geant4 to simulate a certain number of neutrons with an energy of 14 MeV incident vertically from in front of the detector No. 1 to the neutron spectrometer, and the colors represent the number of events. Fig. 25 shows the data measured in this paper under the same conditions. Two bands are evident in both plots when compared, the upper band with a decreasing trend represents those recoil protons that only penetrate detector No. 7 and not detector No. 8, the horizontal coordinate in this case is the total energy of the recoil protons E, and the vertical coordinate is the energy ΔE that the recoil proton loses in detector No. 7 after it penetrates the detector, due to the fact that for the protons with energies higher than 60 keV in the penetration, the energy lost per unit length in Si decreases monotonically with the increase of the proton energy, so the energy lost by the recoil proton in detector No. 7 in this case decreases with the increase of the total energy lost by the recoil proton in both detectors No. 7 and No. 8; the bands with an upward trend in the lower part represent those that have penetrated both detectors No. 7 and No. 8. The lower band with an upward trend represents those recoil protons that penetrate both detector No. 7 and detector No. 8, and the horizontal coordinate in this case is the total energy ΔE2 lost by the recoil protons in detectors No. 7 and No. 8 after they penetrate them, and the vertical coordinate is the energy ΔE1 lost by the recoil protons after they penetrate detector No. 7, and ΔE1 will definitely increase with the increase of ΔE2 in the case of both penetrations.

Due to the difference between the energy and channel correspondences of the two detectors in actual measurements and the effect of the detector energy resolution, the recoil proton bands in the two-dimensional plots of the measured data are not as concentrated as those in the two-dimensional plots of the simulated results, but it is obvious enough to see the relationship between the ΔE of the proton in the Si detector and the total energy E. The results also show that a particle penetrating through more than one detector at the same

time can be extracted from the neutron signal by the back-compliance method. Meanwhile, the experiment also shows that the event of a particle penetrating through multiple detectors can be measured at the same time, which can provide a guarantee for the subsequent extraction of the neutron signal by the inverse conformal method.

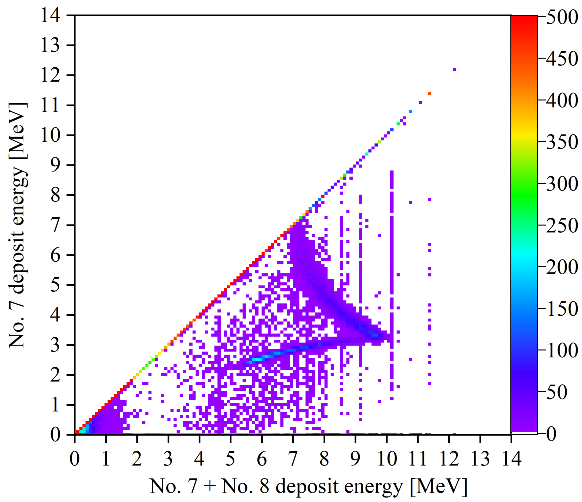

Fig. 24. Simulated data for recoil protons detected by the 14 MeV neutron incident neutron spectrometer

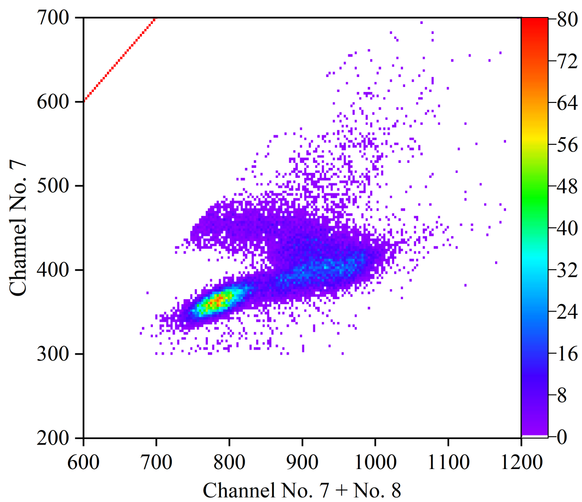

Fig. 25. Recoil proton test data detected by the 14 MeV neutron incident neutron spectrometer

V. SUMMARY

In this paper, a prototype neutron spectrometer payload for LEO neutron detection mission is designed and completed. Starting from the detector combination, two combinations of 15 silicon detectors are used, and the hardware, firmware and software design of the neutron spectrometer is completed. In the process, we have completed the thermal neutron principle test and detection efficiency test by using the nuclear reaction method with 27 μm thick ^{6}LiF as the thermal neutron conversion layer, and the fast neutron principle test and detection efficiency test with 14 MeV and below by using the nuclear recoil proton method with 300 μm thick high-density polyethylene as the fast neutron conversion layer, respectively. And the corresponding simulation analysis of the experiment was carried out, and the experimental data and simulation results are in good agreement and meet the design expectations. The intrinsic detection efficiency of the probes used in neutron spectrometer is 1.05% for 14 MeV fast neutrons. The neutron spectrometer is expected to detect atmospheric albedo neutrons and lightning neutrons in orbit, and to identify lightning neutrons and atmospheric albedo neutrons based on the spatial distribution of lightning occurrences and to obtain the relative contributions of the two.

ACKNOWLEDGMENTS

The authors would like to thank the staff of the "Institutional Center for Shared Technologies and Facilities of INEST, HFIPS, CAS", "Division of Ionizing Radiation Metrology, National Institute of Metrology (NIM), China", CIAE, and CSNS Back-n white neutron facility for the grateful support during the measurement. This work was supported by the National Natural Science Foundation of China (NSFC) through grants numbered 42225405 and U2106202.

[1] B. Klecker, Energetic particle environment in near-Earth orbit. Adv. Space Res. 17, 37-45 (1996). http://dx.doi.org/10.1016/0273-1177(95)00510-L

[2] P. Jiggens, C. Clavie, H. Evans et al., In Situ Data and Effect Correlation During September 2017 Solar Particle Event. Space Weather. 17, 99-117 (2019). http://dx.doi.org/10.1029/2018SW001936

[3] S.F. Singer, Trapped albedo theory of the radiation belt. Phys. Rev. Lett. 1, 300 (1958). https://doi.org/10.1103/PhysRevLett.1.181

[4] M.I. Dobynde, Y.Y. Shprits, Radiation environment created with GCRs inside a spacecraft. Life Sci. Space Res. 24, 116–121 (2020). https://doi.org/10.1016/j.lssr.2019.09.001

[5] Z. Kopal, Physics of the Sun. Br. J. Appl. Phys. 7, 119 (1956). https://doi.org/10.1088/0508-3443/7/4/301

[6] L.Heilbronn, K.Frankel, K.Holabird et al., Production of neutrons from interactions of GCR-like particles. Acta Astronaut. 42, 363-373 (1998). http://dx.doi.org/10.1016/S0094-5765(98)00131-3

[7] L.P. Babich, Generation of neutrons in giant upward atmospheric discharges. Jetp Lett. 84, 285–288 (2006). https://doi.org/10.1134/S0021364006180020

[8] W. Xu, S. Celestin, V.P. Pasko, Monte Carlo simulation of neutron generation by lightning leaders. J. Geophys. Res. Space Physics. 120, 1355-1370 (2015). http://dx.doi.org/10.1109/USNC-URSINRSM.2013.6525017

[9] R.S. Selesnick, M.D. Looper, R.A. Mewaldt, A theoretical model of the inner proton radiation belt. Space Weather 5, 1–19 (2007). https://doi.org/10.1029/2006SW000275

[10] J.F. Valdés-Galicia, Y. Muraki, K. Watanabe et al., Solar neutron events as a tool to study particle acceleration at the Sun. Adv. Space Res. 43, 565–572 (2009). https://doi.org/10.1016/j.asr.2008.09.023

[11] H.Y Huang, Z.Y Zou, J.H Hu et al., Characteristics of radiation belt energetic protons and the movement of their core location in response to geomagnetic disturbances. Phys. Fluids. 36, 076601 (2024). http://dx.doi.org/10.1063/5.0216361

[12] X.L. Li, R.Selesnick, Q. Schiller et al., Measurement of electrons from albedo neutron decay and neutron density in near-Earth space. Nature 552, 382–385 (2017). https://doi.org/10.1038/nature24642

[13] X.X. Yu, H. Lu, G.T. Chen et al., Detection of solar neutron events and their theoretical approach. New Astron. 39, 25–35 (2015). https://doi.org/10.1016/j.newast.2014.12.010

[14] K. Koga, Y. Muraki, S. Masuda et al., Measurement of Solar neutrons on 05 March 2012, using a fiber-type neutron monitor onboard the attached payload to the ISS. Sol. Phys. 292, 115 (2017). https://doi.org/10.1007/s11207-017-1135-y

[15] T. Enoto, Y. Wada, Y. Furuta et al., Photonuclear reactions triggered by lightning discharge. Nature 551, 481–484 (2017). https://doi.org/10.1038/nature24630

[16] L.P. Babich, Radiocarbon Production by Thunderstorms. Geophys. Res. Lett. 44, 11,191-11,200 (2017). http://dx.doi.org/10.1002/2017GL075131

[17] Q.Q. Shi, C.Y. Han, Q.G. Zong et al., Lightning-induced neutrons as a possible source of charged particles in the Earth's inner radiation belt. Earth Planet. Phys., 9(2), 1-8 (2025). http://doi.org/10.26464/epp2025014

[18] J.E. Keith, G.D. Badhwar, D.J. Lindstrom, Neutron spectrum and dose-equivalent in shuttle flights during solar maximum. Nucl. Tracks. Radiat. Meas. 20, 41–47 (1992). https://doi.org/10.1016/1359-0189(92)90083-8

[19] V.E. Dudkin, Y.V. Potapov, A.B. Akopova et al., Differential neutron energy spectra measured on spacecraft in low Earth orbit. Nucl. Tracks. Radiat. Meas. 17, 87–91 (1990). https://doi.org/10.1016/1359-0189(90)90188-4

[20] A.M. Preszler, S. Moon, and R.S. White, Atmospheric neutrons. J. Geophys. Res. 81, 4715–4722 (1976). https://doi.org/10.1029/JA081i025p04715

[21] V.I. Lyagushin, V.E. Dudkin, Y.V. Potapov et al., Russian measurements of neutron energy spectra on the Mir orbital station. Radiat. Meas. 33, 313–319 (2001). https://doi.org/10.1016/S1350-4487(00)00156-6

[22] H. Matsumoto, T. Goka, K. Koga et al., Real-time measurement of low-energy-range neutron spectra on board the space shuttle STS-89 (S/MM-8). Radiat. Meas. 33, 321–333 (2001). https://doi.org/10.1016/S1350-4487(00)00157-8

[23] G.H. Shen, S.Y.Zhang, X.G. Zhang et al., Using Energy Particle Detection Technology on the Tiangong's Space Station's Wentian Laboratory Cabin Module. Aerospace 10, 373 (2023). https://doi.org/10.3390/aerospace10040373

[24] G.H. Shen, D.H Hou, Y. Chang et al., Neutron observations from the energetic particle detector on China's Space Station. Earth Planet. Phys., 9(2), 1-7 (2025). http://doi.org/10.26464/epp2024078

[25] Z.L. Tang, M. Shen, Performance test and evaluation for pixel CdZnTe detector of different thickness. Adv. Mat. Res. 1015, 101–104 (2014). https://doi.org/10.4028/www.scientific.net/AMR.1015.101

[26] L.Y. Liu, X. Ouyang, R.L. Gao et al., Latest developments in room-temperature semiconductor neutron detectors: Prospects and challenges. Sci. China Phys. Mech. Astron. 66, 232001 (2023). https://doi.org/10.1007/s11433-022-2021-6

[27] W. Gao, S. Li, Y. Duan et al., Design and characterization of a low-noise front-end readout ASIC in 0.18-µm CMOS technology for CZT/Si-PIN detectors. IEEE Trans. Nucl. Sci. 65, 1203–1211 (2018). https://doi.org/10.1109/TNS.2018.2826070

[28] S. Zhao, C. Gao, X. Tian et al., A high counting-rate readout ASIC for CZT detectors. Nucl. Instrum. Methods Phys. Res., Sect. A. 1064, 169416 (2024). https://doi.org/10.1016/j.nima.2024.169416

[29] R. He, X.Y. Niu, Y. Wang et al., Advances in nuclear detection and readout techniques. Nucl. Sci. Tech. 34, 205 (2023). https://doi.org/10.1007/s41365-023-01359-0

[30] X. Zhu, C.Q. Feng, Q. Li et al., FPGA-based real-time n/γ discrimination with liquid scintillator. IEEE Trans. Nucl. Sci. 65, 2877–2882 (2018). https://doi.org/10.1109/TNS.2018.2877598

[31] Y.P. Cheng, W.L Guo, Z.Y Tang et al., Mission and Payload Design for In-situ Detection of Lunar Regolith Neutron Radiation Environment. J. Space Sci. Exp. 1, 63–71 (2024). http://dx.doi.org/10.19963/j.cnki.2097-4302.2024.01.007

[32] C.J. Stapels, E.B. Johnson, X.J. Chen et al., Space neutron spectrometer design with SSPM-based instrumentation. Nucl. Instrum. Methods Phys. Res. A. 652, 342–346 (2011). http://dx.doi.org/10.1016/j.nima.2010.10.050

[33] Z.Y. Zhu, M.Q. Pu, M. Jiang et al., Bonding processing and 3D integration of high-performance Silicon PIN detector for ΔE-E telescope. Processes 11, 627 (2023). https://doi.org/10.3390/pr11020627

[34] S.N. Wang, M. Yu, D.Y. Tian et al., Fabrication and characterization of thin Silicon PIN detectors. ECS Trans. 60, 1165 (2014). https://doi.org/10.1149/06001.1165ecst

[35] C.Y. Han, S. Wang, Q.Q. Shi et al., A background suppression detector array for fast neutron measurement in space science study. Measurement 230, 114479 (2024). https://doi.org/10.1016/j.measurement.2024.114479

[36] C.L. Zhou, S.F. Li, C.X Xu, Study on influence factors of the anti-coincidence measuring technique. Nucl. Electron. Detect. Technol. 26, 429–433 (2006). http://dx.doi.org/10.3969/j.issn.0258-0934.2006.04.011

[37] H.M. Gerstenberg, R.S. Caswell, J.J. Coyne, Initial Spectra of Neutron-Induced Secondary Charged Particles. Radiat. Prot. Dosim. 23, 41–44 (1988). http://dx.doi.org/10.1016/S0033-3506(88)80013-1

[38] J.Y. Yang, L. Li, H.W. Lyu et al., A calculation method for parameters of secondary neutron source in nuclear reactor. Nucl. Tech. 41, 060605 (2018). http://dx.doi.org/10.11889/j.0253-

3219.2018.hjs.41.060605

[39] G.H. Zhang, J.M. Liu, Z.H. Xue et al., Measurement of ^{10}B content in thin-film ^{10}B samples. Appl. Radiat. Isot. 69, 858–861 (2011). https://doi.org/10.1016/j.apradiso.2011.02.017

[40] A. Omar, S. Burdin, G. Casse et al., GAMBE: Thermal neutron detection system based on a sandwich configuration of silicon semiconductor detector coupled with neutron reactive material. Radiat. Meas. 122, 121–125 (2019). http://dx.doi.org/10.1016/j.radmeas.2019.01.019

[41] J.S. Wan, G.N. Zhu, Y. Zhao et al., Computer studies of detection efficiency of fast-neutron spectrum based on PADC using the Monte Carlo method. Radiat. Meas. 36, 193–197 (2003). https://doi.org/10.1016/S1350-4487(03)00122-7

[42] Y.M. Ma, Research and design of space neutron detection system. Weihai, China: Shandong University. 2023. https://doi.org/10.27272/d.cnki.gshdu.2023.006159

[43] T.Z. Chen, X.H. Li, K. Wang et al., A readout electronic system for a 3D position-sensitive CdZnTe gamma-ray spectrometer based on the CPRE10-32 readout ASIC. J. Instrum. 17, T10005 (2022). https://doi.org/10.1088/1748-0221/17/10/T10005

[44] C.Y. Han, Simulation and test of neutron spectrometer in near-Earth orbit. Weihai, China: Shandong University. 2022. https://doi.org/10.27272/d.cnki.gshdu.2022.003927

[45] S.Y. Ma, S.B. Liu, H. Liu et al., A SKIROC2-based prototype electronics system for silicon PIN array. Radiat. Detect. Technol. Methods 2, 36 (2018). https://doi.org/10.1007/s41605-018-0060-4

[46] Y.X. Liu, S. Zhang, Y.K. Qian et al., Monte Carlo simulation study on the ^{241}Am-Be radionuclide source reference neutron radiation. Nucl. Technol. Radiat. Prot. 35, 283–293 (2020). https://doi.org/10.2298/NTRP2004283L

[47] W.H. Zhang, H.B. Kang, Y.J. Wang et al., Development of a portable single sphere neutron spectrometer. Radiat. Meas. 140, 106509 (2021). https://doi.org/10.1016/j.radmeas.2020.106509

[48] P.Q. Wang, J.K. Yang, F. Li et al., Thermal neutron reference radiation facility with high thermalization and large uniformity area. Metrologia 60, 45002 (2023). https://doi.org/10.1088/1681-7575/acd6fb

[49] R. García-Baonza, G.F. García-Fernández, E. Gallego et al., A novel conceptualization in the analysis and design of passive neutron area monitors based on gold foil activation. Appl. Radiat. Isot. 181, 110110 (2022). https://doi.org/10.1016/j.apradiso.2022.110110

[50] R. Tursinah, S. Permana, Z. Su'ud et al., Design and validation of a single cylindrical neutron spectrometer using a gold activation foil. Radiat. Meas. 171, 107053 (2024). https://doi.org/10.1016/j.radmeas.2024.107053

[51] W. Jiang, H.Y. Jiang, H. Yi et al., Detector calibration based on secondary protons at the back-n white neutron source. Acta Phys. Sin. 70, 1–18 (2021). http://dx.doi.org/10.7498/aps.70.20201823